THE JOURNAL OF BIOLOGICAL CHEMISTRY VOL. 283, NO. 51, pp. 35689–35702, December 19, 2008

The Apolar Channel in *Cerebratulus lacteus* Hemoglobin Is the Route for O_2 Entry and Exit*

Received for publication, July 25, 2008, and in revised form, September 8, 2008 Published, JBC Papers in Press, October 7, 2008, DOI 10.1074/jbc.M805727200

Mallory D. Salter[‡], Karin Nienhaus[§], G. Ulrich Nienhaus[§¶], Sylvia Dewilde[‖1], Luc Moens[‖], Alessandra Pesce[**], Marco Nardini[‡‡], Martino Bolognesi[‡‡], and John S. Olson[‡2]

*From the [‡]Department of Biochemistry and Cell Biology and the W. M. Keck Center for Computational Biology, Rice University, Houston, Texas 77005-1892, the [§]Institute of Biophysics, University of Ulm, Albert-Einstein-Allee 11, 89081 Ulm, Germany, the [¶]Department of Physics, University of Illinois at Urbana-Champaign, Urbana, Illinois 61801, the [‖]Department of Biomedical Sciences, University of Antwerp, Universiteitsplein 1, 2610 Antwerp, Belgium, the **Department of Physics-CNISM and Center for Excellence in Biomedical Research, University of Genova, Via Dodecaneso 33, 16146 Genova, Italy, and the [‡‡]Department of Biomolecular Sciences and Biotechnology, CNR-INFM and CIMAINA, University of Milano, Via Celoria 26, I-20131 Milano, Italy*

The major pathway for O_2 binding to mammalian myoglobins (Mb) and hemoglobins (Hb) involves transient upward movement of the distal histidine (His-64(E7)), allowing ligand capture in the distal pocket. The mini-globin from *Cerebratulus lacteus* (CerHb) appears to have an alternative pathway between the E and H helices that is made accessible by loss of the N-terminal A helix. To test this pathway, we examined the effects of changing the size of the E7 gate and closing the end of the apolar channel in CerHb by site-directed mutagenesis. Increasing the size of Gln-44(E7) from Ala to Trp causes variation of association (k'_{O2}) and dissociation (k_{O2}) rate coefficients, but the changes are not systematic. More significantly, the fractions ($F_{gem} \approx 0.05–0.19$) and rates ($k_{gem} \approx 50–100\ \mu s^{-1}$) of geminate CO recombination in the Gln-44(E7) mutants are all similar. In contrast, blocking the entrance to the apolar channel by increasing the size of Ala-55(E18) to Phe and Trp causes the following: 1) both k'_{O2} and k_{O2} to decrease roughly 4-fold; 2) F_{gem} for CO to increase from ~0.05 to 0.45; and 3) k_{gem} to decrease from ~80 to ~9 μs^{-1}, as ligands become trapped in the channel. Crystal structures and low temperature Fourier-transform infrared spectra of Phe-55 and Trp-55 CerHb confirm that the aromatic side chains block the channel entrance, with little effect on the distal pocket. These results provide unambiguous experimental proof that diatomic ligands can enter and exit a globin through an interior channel in preference to the more direct E7 pathway.

The structural mechanisms for O_2 binding to myoglobins (Mb)[3] and hemoglobins (Hb) have been the topic of much research since Kendrew (1) and Perutz *et al.* (2) first reported the three-dimensional structures of Mb and Hb over 45 years ago. In the case of mammalian myoglobins, ligand binding is well understood (Refs. 3–10 and references therein) and consists of four major steps. Weakly bound water is displaced to create a vacant distal pocket above the heme iron atom. Ligands migrate into the protein through a short channel that is created when the distal histidine (His-64 at the E7 helical position)[4] transiently rotates upward and then are captured in the interior of the distal pocket. This noncovalent intermediate is often called the B state because it can also be generated by photolysis of the equilibrium bound or A state. Covalent bond formation between the internal ligand and the iron atom of the heme group then competes with ligand escape back out through the His(E7) gate. The bound ligand can be further stabilized by electrostatic interactions with surrounding polar amino acid side chains. This E7 gate pathway appears to occur in most if not all animal hemoglobins, with the classic 3-on-3 α-helical globin fold and a distal histidine, although experimental verification has only been done rigorously for vertebrate Mbs using time-resolved crystallography (4–8), site-directed mutagenesis (3, 9, 11), and time-resolved absorbance and FTIR spectroscopy (12–18).

In contrast, the pathways for ligand binding in truncated 2/2 Hbs (trHbs) appear to be distinct from the E7 gate in the classic 3-on-3 α-helical globins (19–22). These Hbs display loss of elements found in the classic globin fold, including the absence of an N-terminal A helix, significant shortening of the CD corner-D helical region, and reduction of the F helix to an extended polypeptide loop (19, 20, 23). The resulting tertiary structure has the appearance of a 2-on-2 α-helical fold. The abbreviated CD-E region results in the pulling of the E helix closer to the

* This work was supported, in whole or in part, by National Institutes of Health Grant National Institutes of Health Grants GM 35649 and HL 47020. This work was also supported by Robert A. Welch Foundation Grant C-612 (to J. S. O.), Predoctoral Training Fellowship from the Houston Area Molecular Biophysics Training Grant GM 80820 (to M. D. S.), Deutsche Forschungsgemeinschaft Grant Ni 291/3 and the "Fonds der Chemischen Industrie," grants from the Italian Ministry of University and Scientific Research (FIRB Project "Biologia Strutturale" RBLA03B3KC_005) and from the University of Milano (to M. B.), and Fund for Scientific Research Flanders Project "Hypoxia and Nerve Globins" Grant G.0331.04N) (to L. M.). The costs of publication of this article were defrayed in part by the payment of page charges. This article must therefore be hereby marked "*advertisement*" in accordance with 18 U.S.C. Section 1734 solely to indicate this fact.

The atomic coordinates and structure factors (codes 2vyz and 2vyy) have been deposited in the Protein Data Bank, Research Collaboratory for Structural Bioinformatics, Rutgers University, New Brunswick, NJ (http://www.rcsb.org/).

[1] Postdoctoral fellow of the Fund for Scientific Research Flanders Project "Hypoxia and Nerve Globins."

[2] To whom correspondence should be addressed: 6100 Main st., *MS*-140, Houston, TX 77005-1892; Fax: 713–348-5154; E-mail: olson@rice.edu.

[3] The abbreviations used are: Mb, myoglobin; CerHb, *C. lacteus* mini-hemoglobin; k'_{O2}, oxygen association rate coefficient; k_{O2}, oxygen dissociation rate coefficient; K_{O2}, oxygen affinity coefficient; F_{gem}, fraction of geminate recombination; FTIR, Fourier-transform infrared spectroscopy; Hb, hemoglobin; trHb, truncated hemoglobin; WT, wild type; k_{gem}, geminate recombination rate coefficient; TDS, temperature derivative spectroscopy; r.m.s.d., root mean square deviation.

[4] Amino acids have been identified with their topological site numbers as defined in the conventional globin fold.

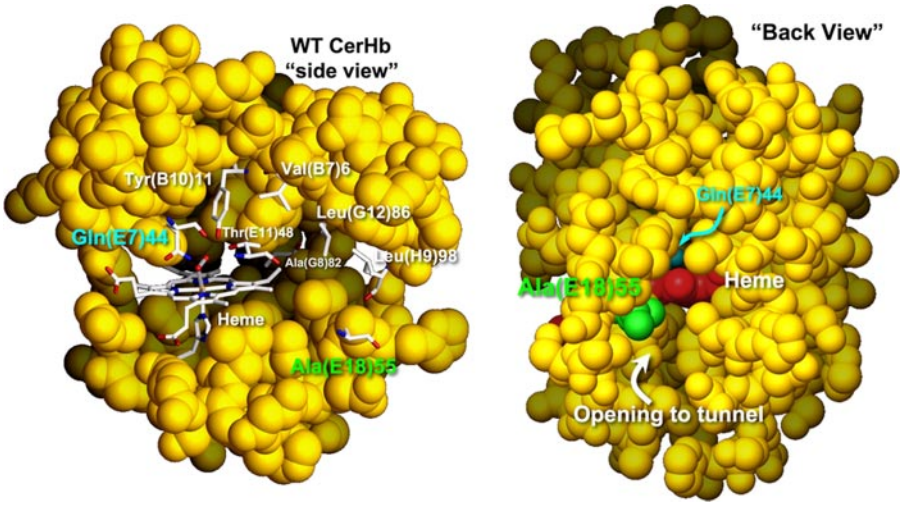

FIGURE 1. **Structure of WT CerHbO_2 (Protein Data Bank code 1KR7) showing side and back views of the molecule.** Gln-44(E7) is labeled in *cyan* and located directly above the heme propionates. Ala-55(E18) is labeled in *green* and located at the end of the E helix forming part of the open entrance to the apolar channel between the E and H helices.

heme distal pocket, which may preclude the use of the E7 residue as a gate for ligand entry and exit. The crystal structures of *Mycobacterium tuberculosis* trHb (trHbN) and other trHbs display the presence of a channel through the protein matrix between the E and H helices, which is large enough for ligand diffusion to the heme distal pocket from external regions near the EF corner and N terminus of the protein (20, 23–27).

An internal apolar channel is also found in the neuronal mini-Hb of the *Nemertean* sea worm, *Cerebratulus lacteus* (28, 29), which, like the trHbs, is missing an A helix. CerHb also has shortened B and H helices (29, 30) making it among the smallest known globins, with only 109 amino acids. CerHb is considered to be in a unique mini-globin subcategory within the larger globin families (29) and has evolved a Mb-like O_2 storage function in the nerve system of the sea worm (30). Like many microbial and invertebrate globins, CerHb has a ligand-binding site containing Tyr(B10) and Gln(E7), which typically evokes an extremely high oxygen affinity because of formation of multiple hydrogen bonds with the bound ligand (28, 31). However, CerHb contains a Thr at the E11 position, and the Thr-48(E11) β-hydroxyl O-γ1 atom pulls the Tyr-11(B10) phenol hydrogen atom away from the bound ligand. As a result, the nonbonding electrons on the Tyr(B10) O-ζ atom are pointing toward the bound ligand, and this negative partial charge causes the oxygen affinity of WT CerHb to be similar to that of vertebrate Mbs ($K_{O2} \approx 1\ \mu M^{-1}$) (31, 32).

CerHb also displays very rapid rates of O_2 association ($k'_{O2} = 240\ \mu M^{-1}\ s^{-1}$) and dissociation ($k_{O2} = 180\ s^{-1}$), which appear to be necessary for rapid gas uptake from oxygenated seawater during surface activity and release to neuronal tissue during periods of hypoxia. These large rate coefficients seem surprising considering the crowded distal pocket and multiple hydrogen bonding interactions that appear to "tie" down the amide side chain of Gln-44, which forms the E7 gate in CerHb. Bolognesi and co-workers (29, 32) have suggested that the large apolar channel between the E and H helices is the pathway for ligand movement into the heme pocket and accounts for the high rates of ligand binding and release. Thus, the loss of the A helix, which blocks access to the channel, may have been an adaptive strategy to allow for rapid rates of O_2 exchange while retaining the Tyr(B10)/Gln(E7) motif.

To test this idea, we have adopted the general mapping strategy described by Scott *et al.* (3) for Mb to examine the extent of ligand movement through the apolar channel in CerHb. The two alternative pathways for ligand movement into and out of CerHbO_2 are shown in Fig. 1. The shortest route to solvent would be through an E7 gate, which in this case would involve outward and upward movement of the Gln-44 side chain. The alternative pathway involves movement in the opposite direction through an apolar channel bounded by Val-7(B6), Ala-55(E18), Ala-82(G8), Leu-86(G12), and Leu-98(H9). We have begun this mapping study by systematically changing the sizes of the amino acids at the entry point of the E7 gate and at the entrance to the apolar channel. Gln-44(E7) has been mutated to Ala, Val, Leu, His, Phe, and Trp, and Ala-55(E18) has been mutated to Val, Leu, Phe, and Trp. The effects of these mutations on overall and geminate rates of O_2 and CO binding have been measured and used to determine the route of ligand entry into CerHb. Low temperature FTIR spectra of the Phe-55 and Trp-55 CerHbCO complexes were measured to determine whether these exterior mutations significantly alter internal rebinding within the distal pocket. Finally, structures of the Phe-55 and Trp-55 CerHbO_2 mutants were determined by x-ray crystallography to ensure that these replacements caused physical blockage of the apolar channel.

EXPERIMENTAL PROCEDURES

Sample Preparation—Wild-type (wt) and mutant recombinant CerHbs were expressed and purified as described previously using a synthetic gene with codon usage optimized for expression in *Escherichia coli* (29, 32). Most recombinant CerHb samples were isolated in the reduced state and used directly. All experiments to determine rate coefficients were carried out in 0.1 M phosphate buffer, pH 7.0, 1.0 mM EDTA, 20 °C. CerHbCO and CerHbO_2 protein samples were prepared by equilibration with 1 atm CO and 1 atm O_2, respectively. When necessary, the unstable Gln-44(E7) mutants were prereduced with dithionite, quickly passed through a G-25 column, and eluted with buffer equilibrated with 1 atm of CO. As noted below, O_2 binding kinetics were often measured in samples containing mixtures of CO and O_2. For those experiments, the starting CerHb sample was in the reduced CO form, which is extremely stable.

Measurement of Overall Rates of Ligand Association and Dissociation—CO association time courses were measured after complete laser photolysis of 50 μM CerHbCO samples containing various [CO] under pseudo first-order conditions.

An ~500-ns excitation pulse from a Phase-R model 2100B dye laser was used for photoexcitation (33, 34), and transmittance changes were recorded with a Tektronix TDS220 digitizing oscilloscope. The time courses were fitted to a simple exponential expression, and k'_{CO} was calculated from the slope of plots of k_{obs} *versus* [CO].

The association rate coefficient for NO binding to deoxy-CerHb was measured using a flow-flash apparatus and the 500-ns dye laser. The flow part of the instrument is composed of a BioLogic SFM400 Multi-Mixer controlled by the MPS-60 Microprocessor. The Multi-Mixer output is connected to the final mixer by a 2-foot water-jacketed umbilical cord containing two flow tubes. This final mixer is part of the base holding a 2-mm fluorescence flow-through cuvette. The excitation and observing beams are focused to intersect at a point in the middle of the quartz cuvette. An anaerobic sample of CerHbCO containing little or no free ligand was mixed with 3/4, 1/2, 1/4, and 1/10 atm NO (1500, 1000, 500, and 200 μM, respectively). Photolysis of the CerHbCO complex was initiated 100 ms after flow stopped and before any significant displacement of CO. Then the complete absorbance change for NO binding to the newly generated deoxy-CerHb was followed at 436 nm. At least four time courses representing new mixtures of CerHbCO and NO were averaged to reduce the signal to noise ratio. This approach avoids the difficulty of photolyzing CerHbNO, which has an extremely small quantum yield. The value of k'_{NO} was determined from the slope of k_{obs} *versus* [NO].

O_2 association and dissociation time courses were determined after complete laser photolysis of CerHbCO samples using the 500-ns dye laser (34, 35). In these reactions, CerHbCO is prepared in buffer containing ~50 μM CO and 1250 μM O_2, 750 μM CO and 250 μM O_2, 500 μM CO and 500 μM O_2, and 250 μM CO and 750 μM O_2. The laser pulse photolyzes the CerHbCO complex, generating deoxy-CerHb, which can then react rapidly with either ligand. The rate of this initial rapid bimolecular rebinding phase, k_{fast}, is monitored by a large decrease in absorbance of unliganded CerHb at 436 nm and is dominated by O_2 rebinding because of its larger association rate coefficient. The value of k_{fast} is given by Equation 1,

$$k_{fast} = k'_{O2}[O_2] + k_{O2} + k'_{CO}[CO] \quad \text{(Eq. 1)}$$

CO dissociation can be neglected because the absolute value of k_{CO} is ~0.01 s^{-1}, whereas under the conditions of the laser experiments, k_{fast} = 10,000–300,000 s^{-1}. The O_2 dissociation rates, k_{O2}, for the WT and mutant CerHbO_2 samples (10–300 s^{-1}, Tables 1 and 2) also make a negligible contribution to the observed rate coefficients for the fast phase.

The slow phase observed after photolysis of CerHbCO in buffer containing mixtures of CO and O_2 represents displacement of the transiently bound O_2 by CO, which, although kinetically less reactive, has a higher affinity for heme (34, 35). The time course of this replacement reaction is best monitored by a large increase in absorbance of CerHbCO at 425 nm. The rate of this process, k_{slow}, is given by Equation 2,

$$k_{slow} = k_{O2}\frac{k'_{CO}[CO]}{k'_{CO}[CO] + k_{O2}[O_2]} \quad \text{(Eq. 2)}$$

An iterative, nonlinear, least squares fitting routine (Solver in Microsoft Excel) was used to optimize the values of k'_{O2}, k_{O2}, and k'_{CO} to give the best fit to the dependence of k_{fast} and k_{slow} on $[O_2]/[CO]$, including conditions where $[O_2] = 0$ and where $[CO] \approx 0$ (34). In previous work, we have shown that this method of using photolysis and O_2/CO mixtures gives results identical to those obtained in more conventional rapid mixing and photolysis experiments, and eliminates problems because of autooxidation of unstable mutants and low HbO_2 quantum yields (35).

CO dissociation time courses were determined by stopped-flow analysis in which the heme-bound CO was displaced by a high concentration of the higher affinity NO ligand. In these experiments, 5–10 μM CerHbCO samples are mixed with 1 atm NO (2000 μM), and the decrease in CerHbCO is monitored at 420 nm (33, 36). Under these conditions, the observed first-order rate constant is directly equal to k_{CO}.

Measurement of Geminate Recombination—Time courses for internal rebinding within CerHb were measured at 436 nm after excitation with a 9-ns excitation pulse from a Lumonics YAG-laser system, using a Tektronix TDS3052 digitizing oscilloscope on nanosecond time scales. The geminate rebinding time courses were fitted to one or two exponential expressions with an offset reflecting the amount of escape to solvent (3). For a simple exponential rebinding process, the fraction of geminate recombination, F_{gem}, was calculated as $F_{gem} = (\Delta A_{gem}/\Delta A_{gem} + y_0)$, where ΔA_{gem} represents the absorbance change associated with internal geminate rebinding (one or two phases), and y_0 (the offset) is the difference between the absorbance after complete geminate recombination and the absorbance of the original ground state, which is observed prior to photolysis or at long times after bimolecular rebinding from solvent is complete (*i.e.* fully liganded CerHb). The observed rates of geminate rebinding, k_{gem}, were independent of ligand concentration.

Crystallization and X-ray Diffraction Data Collection—Purified Phe-55 and Trp-55 CerHb mutants were crystallized by vapor diffusion techniques (protein concentration 27 mg/ml) under conditions matching those for crystallization of the WT protein (28). In both cases, elongated prismatic crystals (about $0.04 \times 0.04 \times 0.2$ mm^3) grew within 2 weeks. The crystals were stored in 2.8 M ammonium sulfate, 50 mM sodium acetate, pH 6.0, and transferred to the same solution supplemented with 15% glycerol (v/v) (cryo-solution) immediately before data collection at 100 K. All x-ray diffraction data were collected at the ESRF synchrotron facility (beam line ID14-1, Grenoble, France) and processed using MOSFLM and SCALA (40, 41). Phases were calculated by molecular replacement methods with the program MOLREP (42), as implemented in the CCP4 program package (43, 44), using the WT oxygenated structure as a starting model (Protein Data Bank accession code 1KR7 (29)). The mutant CerHb crystal structures were refined using REFMAC (45) and models inspected and modified using COOT (46). *B*-factors have been refined isotropically for the 1.8 Å data of the Phe-55 mutant and anisotropically for the high resolution 1.6 Å data of the Trp-55 mutant. Atomic coordinates and structure factors for Phe-55 and Trp-55 CerHb mutants have been

TABLE 1

Rate and equilibrium constants for O_2 and CO binding to position 44(E7) mutants of CerHb at pH 7.0, 20 °C

Two phases of roughly equal amplitudes were observed for O_2 association with and dissociation from Trp-44 CerHb, and rate parameters for each phase are reported.

Mutants	k'_{O2}	k_{O2}	K_{O2}	k'_{CO}	k_{CO}	K_{CO}	M (K_{CO}/K_{O2})
	$\mu M^{-1} s^{-1}$	s^{-1}	μM^{-1}	$\mu M^{-1} s^{-1}$	s^{-1}	μM^{-1}	
Ala-44	160 (180)[a]	33 (30)[a]	4.9 (6.0)[a]	41 (40)[a]	0.05, 0.0004	820, 10000	170, 2100
Val-44	130	84	1.5	25	0.032	780	510
Leu-44	184 (200)[a]	96 (96)[a]	1.9 (2.1)[a]	36 (42)[a]	0.016	2200	1200
Gln-44(E7) WT	**230 ± 17**	**190 ± 25**	**1.2 ± 0.2**	**32 ± 4.7**	**0.054 ± 0.005**	**590 ± 100**	**490 ± 110**
His-44	85 (130)[a]	81 (65)[a]	1.0 (2.0)[a]	4.0 (5.3)[a]	0.010	400	380
Phe-44	20 (23)[a]	170 (170)[a]	0.11 (0.14)[a]	1.3 (1.6)[a]	0.054	24	210
Trp-44	10, 170	330, 33	0.03, 5.2	5	0.035, 0.011	140, 460	4600, 89

[a] The rate constants given in parentheses were measured previously with different preparations of position 44 mutants and were described in Refs. 21,32. The standard deviations for the WT values for k'_{O2}, k_{O2}, and k'_{CO} were obtained from the analysis of 12 completely independent sets of experiments starting with at least 7 different expressions and purifications of CerHb. The standard deviation for k_{CO} came from the analysis of 16 different determinations. The values of K_{O2} and K_{CO} were calculated from k'_{O2}/k_{O2} and k'_{CO}/k_{CO}, and their standard deviations were calculated from the standard propagation of error formula.

deposited with the Protein Data Bank (47) with accession codes 2vyz and 2vyy, respectively.

Fourier Transform Infrared (FTIR) Temperature Derivative Spectroscopy (TDS)—FTIR-TDS is an experimental method designed to investigate thermally activated rate processes (12, 37, 38). The apparatus, method, and aspects of data collection have been described in general (39), and specific details for CerHbCO samples are presented in Pesce *et al.* (32) and Deng *et al.* (21). Briefly, the sample is cooled to an initial temperature at which the rebinding of CO is preferentially arrested on the experimental time scale of minutes to several hours (typically 3 K). Photolysis creates a nonequilibrium state, and the recovery of the bound state is measured as the temperature is slowly increased. FTIR-TDS data are presented as two-dimensional contour plots on a surface spanned by temperature and wave number axes (see Fig. 8).

RESULTS

Effects of Position 44 (E7) Mutations on Overall O_2 and CO Binding—Bimolecular association (k') and unimolecular dissociation (k) rate coefficients for ligand binding to Gln-44(E7) mutants of CerHb are listed in Table 1. Some of these rate parameters were reported in previous publications (21, 32). We constructed the Val-44 mutant to complete the series of size variants at the E7 gate position and re-measured all the O_2 and CO binding parameters for direct comparison with the same replacements in sperm whale Mb, which uses the E7 gate for ligand entry and exit (Fig. 2).

In general, replacement of His-64(E7) with smaller apolar amino acids (Ala, Val, and Leu) in Mb results in dramatic increases in both k'_{O2} and k_{O2}. In the case of ligand association, the 5–10-fold increases are due to loss of noncovalently bound water and opening of the E7 channel, both of which increase the rate of ligand entry into Mb. In the case of dissociation, the large 100–1000-fold increases in k_{O2} are because of loss of hydrogen bonding to bound O_2, causing greater rates of thermal Fe–O_2 bond breakage. The increases in k_{O2} dominate, resulting in large ~100-fold decreases in O_2 affinity for the apolar E7 mutants of Mb (K_{O2} values Fig. 2*C*).

In contrast to Mb, replacing Gln-44(E7) with small apolar amino acids in CerHb results in decreases in the rates of both O_2 association and dissociation and small increases in O_2 affinity (Ala, Val, and Leu, *solid bars* in Fig. 2). The decreases in k'_{O2} and k_{O2} with decreasing size and polarity at the E7 position argue against this amino acid being part of the pathway for entry and exit because opposite effects, increases in k'_{O2} and k_{O2}, would be expected if the E7 channel were enlarged and made apolar, and the side chain gate was removed. As shown in Fig. 2*A*, there are significant decreases in the bimolecular rate for O_2 binding when the size of the E7 amino acid is increased from Gln to His, Phe, and Trp. However, there are no large concomitant decreases in the O_2 dissociation rate coefficient, and as a result, there are significant ~10-fold decreases in O_2 affinity for the larger Phe-44 and Trp-44 CerHb mutants (Table 1). These effects for the larger 44(E7) amino acids appear to be due to direct side chain interactions with the bound ligand and not alterations in the speed of entry and escape.

The Trp-44 CerHb mutant shows two distinct and roughly equal phases for O_2 association, O_2 dissociation, and CO dissociation (Table 1). The slower phase for O_2 association shows a rate similar to that for binding to the Phe-44 mutant, whereas the faster phase is similar to that of Ala-44 CerHb. The simplest interpretation is that the indole side chain can occupy an inward orientation that directly hinders binding to the iron atom and an outward orientation that leaves the iron more accessible, regardless of the pathway for ligand entry and exit. The low k'_{O2} value would correspond to the inward conformer, and the high k'_{O2} value would correspond to the outward conformer. Using this steric hindrance model, we assigned the high rate of O_2 dissociation to the inward conformer, in which the large indole side chain sterically hinders bound ligands and enhances the rate of iron-ligand bond breakage. For this interpretation, the calculated O_2 affinity of the inward conformer would be 0.03 μM^{-1}, which is similar to that for the Phe-44 CerHb mutant. The outward conformer would have K_{O2} = ~5 μM^{-1}, which is similar to the affinity of the unhindered Ala-44 mutant. Although these assignments are compelling, they must be considered tentative in the absence of a crystal structure of the Trp-44(E7) mutant and further investigation.

Geminate CO Recombination in 44(E7) Mutants—Although the overall kinetic parameters in Table 1 indicate that Gln-44(E7) is not acting as a gate for ligand entry and exit, the results are complex and difficult to interpret unambiguously. To explore the role of this position more completely, we measured time courses for geminate CO recombination in all six 44(E7) CerHb mutants (Fig. 3*A*). In this case, the results are definitive. Neither the rate nor the extent of geminate recombination vary

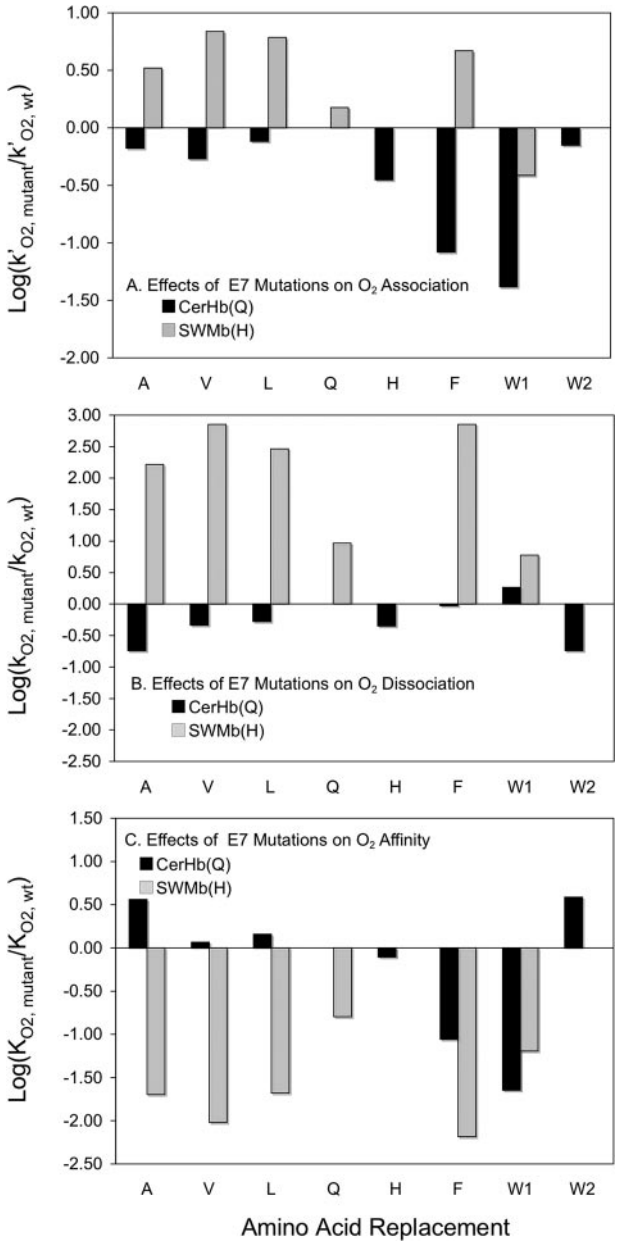

FIGURE 2. **Comparison of the effects of E7 mutations on the association, dissociation, and equilibrium constants for O_2 binding to sperm whale Mb (3, 33) and CerHb.** The WT amino acids are His-64(E7) and Gln-44(E7) in Mb and CerHb, respectively, and the effects are expressed as the logarithm of the ratio of the mutant parameter divided by the WT parameter. All samples were prepared in 0.1 M phosphate, pH 7, and rates were measured at 20 °C. O_2 binding to Trp-44 CerHb showed two phases of roughly equal amplitudes. We assigned *W1* to the slow component with reduced association and dissociation rate constants and *W2* to the faster reacting component. In contrast, sperm whale Trp64 showed only a single slow phase, and its values are presented as *W1*.

widely with increasing size, from Ala to Trp-44, supporting the idea that the amino acid at the E7 position is not part of the gate for ligand movement into the distal pocket of CerHb.

The largest fraction of geminate recombination is 0.19 (Leu-44), and the smallest is ~0.02 (Phe-44), with WT CerHb (Gln-44) being 0.05. The rates of geminate recombination (k_{gem}) do not vary greatly, 60 to ~100 μs^{-1}, and because the extent of geminate recombination is small (≤20%), the values of k_{gem} represent the rates of escape from the CerHb mutants (see under "Discussion" and Equation 3). Thus, it is clear that changes in the size of the position 44(E7) amino acid have little effect on ligand escape. In contrast, Scott *et al.* (3) observed systematic increases in the fraction of O_2 geminate rebinding with increasing size of the E7 position in Mb, from ~0.12 for Ala-64 to 0.72 for Trp-64.

O_2 and CO Binding to Position 55(E18) Mutants—As shown in Fig. 1, Ala-55(E18) is located at the exit and entry point of the apolar channel between the E and H helices. To see if this entrance could be blocked, Ala-55(E18) was replaced with Val, Leu, Phe, and Trp, with the premise that the barrier to ligand uptake would increase with increasing size of the amino acid side chain. As shown in Fig. 4 and Table 2, there are strong inverse correlations between amino acid size and the rates of O_2 association and dissociation, with both k'_{O2} and k_{O2} decreasing by >3–4-fold for the Ala-55(E18) to Leu, Phe, and Trp mutations and little change in K_{O2}. The concomitant decreases in k'_{O2} and k_{O2} suggest strongly that the mutations are increasing the free energy barrier for entering the protein and only affecting this transition state. This pattern of effects is in contrast to the more complex behavior seen when the size of the amino acid at position 44(E7) is increased (Fig. 4*C versus* Fig. 2).

As shown in Table 2, the affinity of CerHb for O_2 shows almost no dependence on the size of the amino acid at position 55(E18). This observation argues strongly that the mutations only affect movement into the apolar channel, and this conclusion is supported by the much smaller effects observed for CO association and dissociation. In most globins, CO binding is limited by the rate of internal bond formation or bond breakage and not movement into and out of the protein (48, 49). As a result, the overall CO association and dissociation rate coefficients are little affected by mutations that only affect entry and exit into the protein, as is observed for the position 55(E18) mutants (Table 2, part B).

Effects of Position 55 Mutants on Geminate Recombination—Replacing Ala-55(E18) with larger amino acids increases the fraction of geminate recombination, F_{gem}, for both O_2 and CO but slows the rate, k_{gem}, markedly (Fig. 3, *B* and *C*, and Table 2). In the case of CO geminate rebinding, F_{gem} increases almost 10-fold, from 0.05 to 0.44, whereas k_{gem} decreases ~10-fold from ~80 to ~9 μs^{-1}. Similar increases in F_{gem} and decreases in k_{gem} occur for internal O_2 rebinding, but in this case the values are more difficult to assign because extensive geminate recombination is occurring during excitation and at speeds approaching the decay rate of the laser pulse. However, the trends are identical to those seen for CO rebinding. The key observation is that the rate of geminate recombination decreases, whereas the fraction of rebinding increases as the channel is blocked.

These trends demonstrate that the increase in geminate rebinding is because of slowing of escape and not an increase in the rate of internal bond formation. The observed decay rate of the nanosecond intermediate is equal to the sum of the rate of internal Fe(II)-ligand bond formation and the rate of ligand escape. The fraction of geminate rebinding is given by the ratio of the rate of bond formation divided by the sum of the rates of bond formation and escape. F_{gem} for WT CerHb is very small, indicating the rate of ligand escape must be much larger than

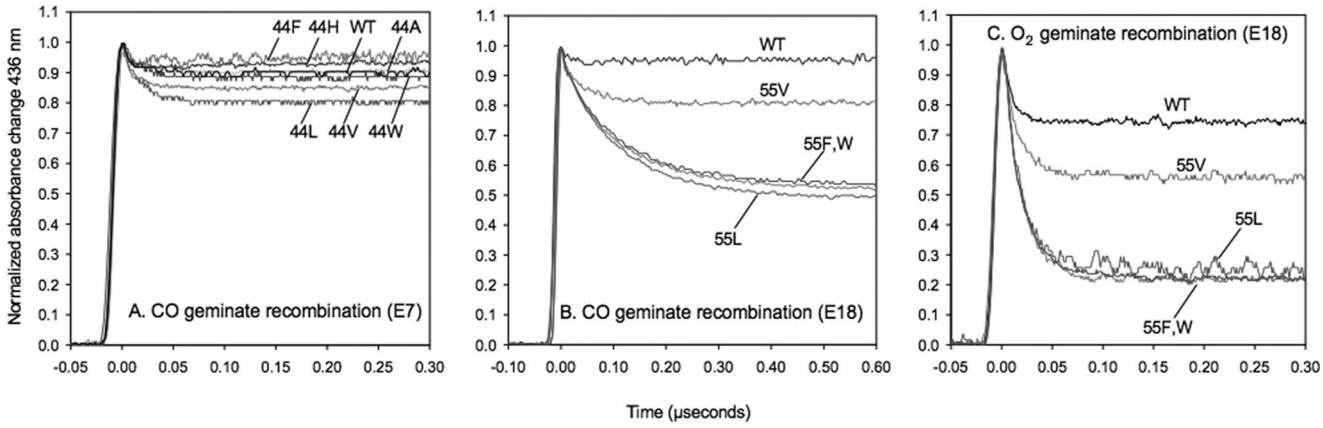

FIGURE 3. **Time courses for geminate recombination in mutants of CerHb at 20 °C, pH 7.0.** *A*, geminate rebinding in position Gln-44(E7) mutants of CerHbCO. *B*, CO geminate rebinding in position Ala-55(E18) mutants. *C*, O_2 geminate rebinding in position Ala-55(E18) mutants.

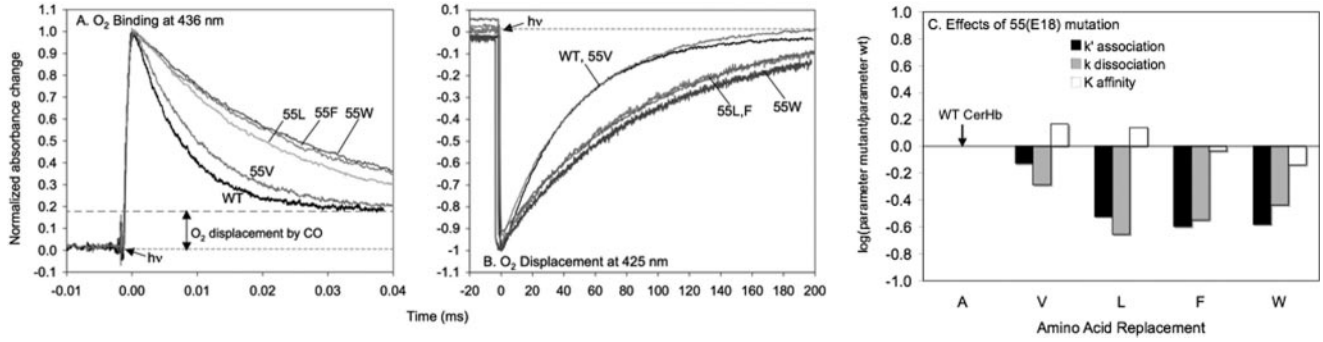

FIGURE 4. **Time courses for O_2 binding to WT and 55(E18) mutants of CerHb at pH 7, 20 °C.** *A*, bimolecular rebinding measured at 436 nm after photolysis of a mixture of 50 μM CerHbCO at 1250 μM O_2, conditions in which bimolecular O_2 rebinding dominates. *B*, slow O_2 displacement phase measured at 425 nm after photolysis of a mixture of 50 μM CerHbCO, 500 μM CO, and 625 μM O_2, conditions in which O_2 dissociation is the primary determinant of the observed rate. *C*, summary of the effects of the 55(E18) mutations. The expressions used to calculate the association and dissociation rate coefficients for O_2 binding and dissociation are given in Equations 1 and 2. The logarithm of the ratio of the mutant parameter to the WT parameter is plotted *versus* amino acid size for the series Ala, Val, Leu, Phe, and Trp.

TABLE 2

Rate, equilibrium, and geminate constants for O_2 and CO binding to position 55(E18) mutants of CerHb at pH 7, 20 °C

Mutant	Bimolecular binding parameters			Observed geminate parameters	
	k'_{O2}	k_{O2}	K_{O2}	k_{gem}	F_{gem}[a]
	$\mu M^{-1} s^{-1}$	s^{-1}	μM^{-1}	μs^{-1}	
A. O_2 binding at pH 7.0, 20 °C					
Ala-55 WT	230 ± 17	190 ± 25	1.2 ± 0.2	(~130)	0.39
Val-55	180	93	1.9	64	0.58
Leu-55	72	40	1.8	54	0.83
Phe-55	61	51	1.2	55	0.86
Trp-55	63	66	0.95	55	0.86
Mutant	**Bimolecular binding parameters**			**Observed geminate parameters**	
	k'_{CO}	k_{CO}	K_{CO}	k_{gem}	F_{gem}
	$\mu M^{-1} s^{-1}$	s^{-1}	μM^{-1}	μs^{-1}	
B. CO Binding at pH 7.0, 20 °C					
Ala-55 WT	32 ± 4	0.054 ± 0.005	590 ± 100	(~80)	0.05 ± 0.03
Val-55	41	0.045	910	24	0.16
Leu-55	17	0.016	1100	7.6	0.46
Phe-55	17	0.029	590	9.3	0.44
Trp-55	14	0.029	500	9.4	0.44

[a] The fraction of geminate O_2 rebinding to CerHb was estimated by assuming a "dead time" of 9 ns for the laser light pulse. This adjustment partially compensates for the amount of geminate rebinding that occurs during the laser pulse but is only an approximation. The standard deviations for the overall rate coefficients for WT CerHb are described in Table 1, and the relative errors are approximately ±10% for ≥12 completely independent measurements and are assumed to apply to the parameters for 55(E18) mutants. The standard deviation for F_{gem} for WT CerHbCO was taken from six independent measurements.

the rate of internal bond formation. Consequently, the observed rate of the small geminate phase is roughly equal to the speed of escape, which then decreases as the larger 55 mutations inhibit exit from the apolar channel. Eventually, the rate of escape becomes roughly equal to the rate of internal bond formation, and then the extent of internal rebinding is ~50%. This interpretation is described quantitatively under "Discussion" (see Equations 3 and 4).

Association Rate Coefficients for NO Binding—The bimolecular rate of NO binding to globins is determined solely by the rate of entry into the protein because, once captured in the distal pocket, virtually all the internal ligands bind to the iron atom before escaping because of the highly reactive, free radical nature of NO. This high reactivity accounts for the large extent of picosecond geminate rebinding of NO in photolysis experiments, the very low overall quantum yield of NO complexes (≤0.01), and the large bimolecular association rate coefficients for NO binding, k'_{NO} (48). Scott *et al.* (3) have shown that there is a 1:1 correlation between the bimolecular rate of ligand entry, k'_{entry}, calculated from a combined analysis of geminate and overall O_2 rate coefficients and the values of k'_{NO} determined for over 90 different sperm whale Mb mutants. Thus, rates of NO binding to the position 55(E18) mutants of CerHb were measured to examine more directly if the larger amino acids are slowing the rate of ligand entry. As shown in Fig. 5 and Table 3, the rate of NO binding decreases over 5-fold when Ala-55 is replaced with Leu, Phe, and Trp, and the values of k'_{NO} are similar to those for k'_{O2} implying that the rate-limiting step for O_2 binding is also movement into the protein and through the channel (see also Table 3 and under "Discussion").

Crystal Structures of Phe-55 and Trp-55 CerHb—The crystal structures of the Trp-55 and Phe-55 mutants were determined to visualize whether the large aromatic side chains do block the entrance to the apolar channel and to examine whether perturbations of the distal pocket occur because of changes at the EF corner of the CerHb tertiary structure. The three-dimensional structures of Phe-55 and Trp-55 CerHbO_2 were refined to final *R*-factor/*R*-free values of 18.8/23.0% and 16.7/21.3%, respectively, at 1.8 and 1.6 Å resolution, with good overall stereochemistry (Table 4).

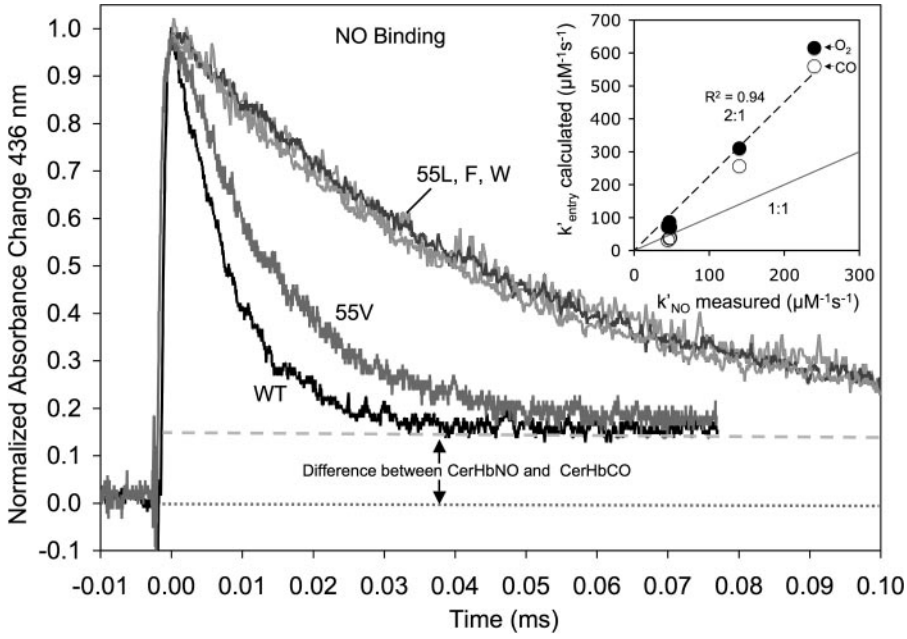

FIGURE 5. **NO binding to 55(E18) mutants of CerHb at pH 7, 20 °C.** CerHbCO (~50 μM) was rapidly mixed with buffer equilibrated with 1 atm of NO, and photolysis was initiated immediately afterward to generate deoxy-CerHb in ~0.5 μs. NO binding was followed at 436 nm. The offset is because of the difference in absorbance between the initial CerHbCO and final CerHbNO complexes. This experiment was repeated with four different NO concentrations, and k'_{NO} was determined from the slope of plots of k_{obs} *versus* [NO]. *Inset*, correlations between the calculated value of k'_{entry} and the measured value of k'_{NO} for WT and the four 55(E18) mutants.

The overall tertiary structures of the mutant proteins are unaffected by the mutations at position 55(E18) (Fig. 6*A*). The r.m.s.d. calculated between the C-α atoms of the WT and mutated proteins is 0.15 Å for both mutants, and only marginal readjustments can be detected at the end of the E helix and along the adjacent H helix (residues 97–104) because of the larger aromatic side chains at position 55(E18). When the two mutant structures are superimposed (overall r.m.s.d. of 0.13 Å), the phenyl ring of Phe-55 sits approximately in the center of mass of the indole ring of Trp-55 (Fig. 6*A*). The Phe and Trp side chains make 19 and 26 favorable van der Waals contacts, respectively, with adjacent regions of the protein, and the Trp-55(E18) indole N-δ1 atom appears to form a weak hydrogen bond with the O-δ2 atom of

TABLE 3

Bimolecular rate coefficients for NO binding and calculated rate parameters for entry, escape and internal bond formation for position 55(E18) mutants of CerHb using the simple two step mechanism shown in Fig. 9 and Equations 3 & 4

CerHb	k'_{NO}	Calculated rate parameters for two-step mechanism			
		k'_{entry}	k_{escape}	K_{entry}	k_{bond}
	$\mu M^{-1} s^{-1}$	$\mu M^{-1} s^{-1}$	μs^{-1}	M^{-1}	μs^{-1}
A. Kinetic parameters derived from NO and CO binding at pH 7.0, 20 °C					
Ala-55 (WT)	240	560	76	7	4.0
Val-55	140	260	20	13	3.8
Leu-55	47	37	4	9	3.5
Phe-55	48	39	5	8	4.0
Trp-55	45	32	5	6	4.1
B. Kinetic parameters derived from O_2 binding at pH 7.0, 20 °C					
Ala-55 (WT)	240	620	79	8	51
Val-55	140	310	27	12	37
Leu-55	47	87	9	9	45
Phe-55	48	71	8	9	47
Trp-55	45	73	8	10	47

TABLE 4
X-ray data collection, refinement statistics, and model quality

	Phe-55 (E18) CerHbO_2	Trp-55 (E18) CerHbO_2
Data collection		
Space group	$P2_12_12_1$	$P2_12_12_1$
Cell dimensions	a = 42.88 Å, b = 43.35 Å, c = 59.88 Å	a = 42.79 Å, b = 43.32 Å, c = 60.04 Å
Resolution	43.36-1.80 Å (1.90-1.80)[a]	43.31-1.60 Å (1.69-1.60)
Observations	41,523	52,593
Unique reflections	10,801	15,251
Completeness	99.6 (99.7)%	99.7 (99.9)%
R-merge[b]	12.0 (28.2)%	6.4 (31.5)%
$I/\sigma(I)$	9.5 (4.1)	12.7 (4.1)
Multiplicity	3.8 (3.9)	3.4 (3.4)
Refinement		
R-factor/R-free	18.8/23.0%	16.7/21.3%
Protein atoms in the asymmetric unit	829 (residue 0–109)	839 (residue 0–109)
Side chains with alternative conformations	Ser-34, Gln-44	Lys-16, Ser-34, Gln-44, Ser-76
Dioxygen molecules	1	1
Water molecules	145	160
Sulfate ions	1	2
Acetate ions	1	0
Glycerol	2	0
Model quality		
Overall B-factor	13.7 Å^2	13.7 Å^2
r.m.s.d.[c] from ideal values		
Bond lengths (Å)	0.013 Å	0.010 Å
Bond angles (°)	1.245°	1.080°
Ramachandran plot[d]		
Most favored regions	94.7	96.8
Additional allowed regions	5.3	3.2

[a] Outer shell statistics are shown within parentheses.
[b] R-merge $= \Sigma_h \Sigma_i |I_{hi} - \langle I_h \rangle| / \Sigma_h \Sigma_i \langle I \rangle_{hi}$.
[c] r.m.s.d. is root mean square deviation.
[d] Data were produced using the program PROCHECK (63).

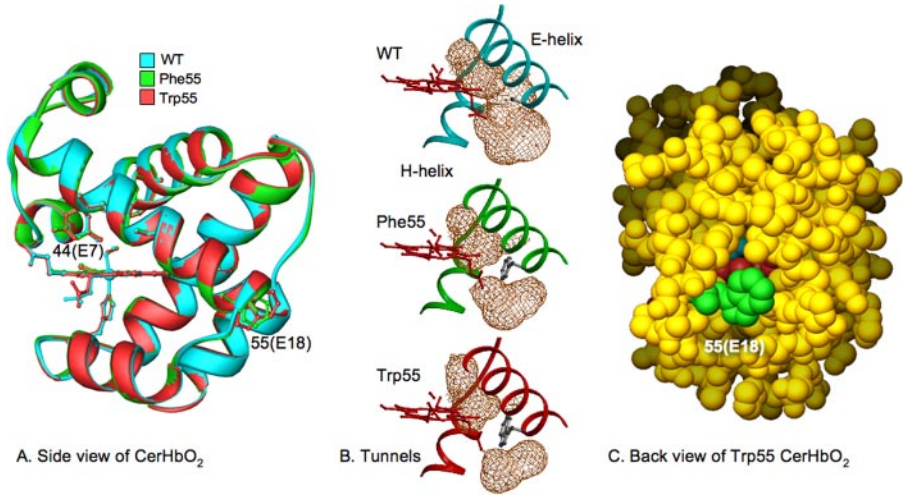

FIGURE 6. **Comparison of WT CerHbO_2 and 55(E18) mutant structures.** *A,* overlay of ribbons drawings of WT (*cyan*), Phe-55 (*green*), and Trp-55 (*red*) CerHb. The same amino acid side chains shown in Fig. 1*A* are presented as *sticks* in this drawing, but only the E7 and E18 positions are labeled and show different positions. *B,* disruption of the apolar channel at the end of the E helix by the Phe-55 and Trp-55 mutations. Protein cavities were calculated with a 1.4-Å radius probe using the program SURFNET (50) and are represented as a *brown network*. Side chains of the mutated residues at position 55(E18) are shown in *ball-and-stick* representation. *C,* "back" space-filling view of Trp-55 showing that the indole ring (*green*) blocks the entrance to the apolar channel. This structure should be compared with the same view of WT CerHbO_2 in Fig. 1*C*.

Asp-104(H15). The Phe-55 and Trp-55 side chains fit into a cleft, located between the end of the E helix and the beginning of the H helix, bordered by surface residues His-100(H11), Asp-104(H15), and by main chain carbonyl groups of the 55–62 region (EF helical corner, Figs. 1 and 6). In WT CerHb this cleft is "open" and provides access to the elongated channel, lined by the hydrophobic residues Val-7(B6), Phe-10(B9), Ile-52(E15), Ala-55(E18), Leu-86(G12), Leu-98(H9), Ala-101(H12), Ile-102(H13), and Ile-105(H16), by the hydrophilic residues Tyr-11(B10), Thr-48(E11), and Tyr-51(E14), and by the heme B-methyl and B-vinyl groups (Fig. 1*A*). The surface aperture of the cleft is bordered by residues Ala-55(E18), Ala-60(F1), Ala-62(F2), and Asp-104(H15) and has a diameter of between 6.8 and 7.7 Å. Thus, the major structural effect of the Ala-55(E18) to Phe and Trp mutations is blocking access to the channel from the solvent phase (Fig. 6*C*).

The blockage caused by the Ala-55(E18) mutations is shown in Fig. 6*B*, where protein cavities were calculated using a 1.4-Å radius probe (50) and is depicted as *brown mesh* networks. In WT CerHb, the apolar channel connects directly to the aperture between the E and H helices. In contrast, the entrance is almost fully blocked by the aromatic rings of the Phe-55 and Trp-55 side chains. The interior channel in the mutants appears as an isolated cavity of roughly the same size (57 Å^3) as that found in the internal channel of the WT protein (59 Å^3). In both mutants and WT CerHb, the lower portion of the channel entrance hosts two water molecules hydrogen-bonded to each other and the Ala-101(H12) carbonyl O atom, the Tyr-51(E14) hydroxyl, and the O-δ2 atom of Asp-104(H15). The aromatic substitutions cause only minor alterations in the

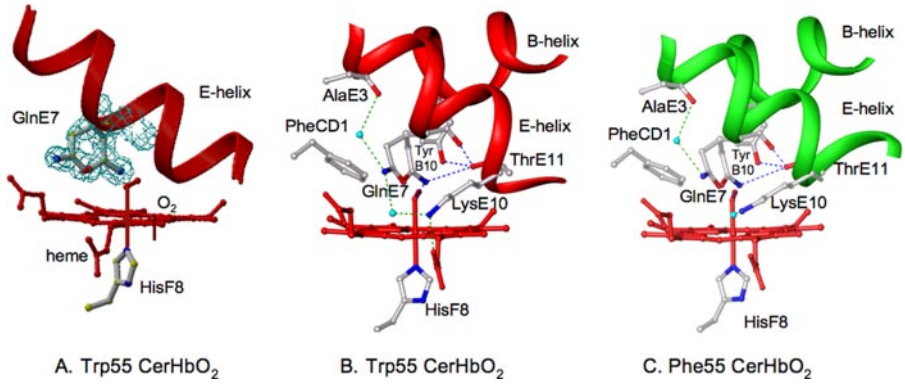

FIGURE 7. **The distal pockets of the Trp-55 (*A* and *B*) and the Phe-55 (*C*) mutants.** Residues Phe-10(B9), Tyr-11(B10), Phe-25(CD1), Ala-40(E3), Gln-44(E7) (two side chain conformations), Lys-47(E10), and Thr-48(E11), the dioxygen molecule (*red*), the heme group, and part of the polypeptide chain path are shown in *ball-and-stick* and *ribbon* representations. The proximal His(F8) residue and selected water molecules are also shown. Hydrogen bonds within the distal pocket are drawn as *dashed blue lines*, and external hydrogen bonds are drawn as *green dashed lines*. External water molecules are shown as *small cyan spheres*. Weak electrostatic interactions may also occur between the innermost Gln-44(E7) atom and the Tyr-11(B10) hydroxyl but are not shown.

positions of these water molecules, which are not located within the apolar channel.

Multiple Conformations of Gln-44(E7)—Even though there appear to be few changes in the positions of the C-α atoms in the N-terminal region of the E helix and the CD corner (Fig. 6*A*), the amide side chain of Gln-44(E7) is found in two conformations in both the Phe-55 and Trp 55 mutant structures (Fig. 7). The electron density clearly defines two positions of roughly equal occupancy, which will affect electrostatic fields near the iron atom and could potentially influence the rates of O_2 binding and the FTIR spectra of bound CO. This double conformation is particularly well defined in the Trp-55 CerHbO$_2$ structure, perhaps because of the higher resolution of the x-ray diffraction data for this mutant (1.6 Å). The innermost Gln-44(E7) conformer exactly matches the rotamer found in the oxygenated WT protein and appears to form a hydrogen bond between the Gln-44(E7) N-ϵ2 atom and the O-1 of the bound ligand (O-1–N-ϵ2 distances of 2.61 and 2.66 Å in the Phe-55 and Trp-55 mutants, respectively). The Gln-44(E7) N-ϵ2 atom may also weakly interact with the Tyr-11(B10) hydroxyl O-ζ atom (distances of 3.26 and 3.28 Å in the Phe-55 and Trp-55 mutants, respectively) and with the Thr-48(E11) O-γ1 atom (distances of 3.36 and 3.25 Å in the Phe-55 and Trp-55 mutants, respectively).

Note that in all the structures, the Thr-48(E11) O-γ1 atom is accepting a strong hydrogen bond from the hydroxyl proton of Tyr-11(B10) (2.48 and 2.56 Å in Phe-55 and Trp-55 CerHbO$_2$, respectively). Thus, all bound ligands are experiencing a partial negative charge from the nonbonded electrons of the O-ζ atom of Tyr-11(B10), which accounts for the moderate O_2 affinity (Table 2) and high stretching frequency of bound CO (~1980 cm^{-1}, Fig. 8) (21, 32) for WT CerHb and all five position 55 mutants. A complete discussion of the key role of Thr-48(E11) in regulating O_2 binding in CerHb is given in Pesce *et al.* (32).

In the second outermost conformation, the Gln-44 (E7) side chain is rotated by about 180° toward the solvent interface (Fig. 7). As a consequence, polar interactions with the bound ligand, Tyr-11(B10), and Thr-48(E11), are lost. However, in the outer conformation of Trp-55 CerHbO$_2$, the Gln-44(E7) N-ϵ2 atom appears to be part of a hydrogen bonding network, which connects the carbonyl of Ala-40(E3) to the N-ζ of Lys-47(E10) through well defined water molecules, and there may also be electrostatic interactions with the heme propionates. This network is less well defined in the Phe-55 structure.

The outward rotation of Gln-44(E7) in the 55 mutants is puzzling for four reasons. First, it is not clear how mutations at the end of the E helix cause this conformational shift of the E7 side chain without causing a significant change in the position 44 C-α atom. A simple interpretation would be that the larger Phe-55 and Trp-55 side chains sterically clash with their surroundings altering the dynamics of the MACROS BELOW ARE FOR THE VISUALE-helix that allows two conformations for the Gln-44 side chain, but this idea remains speculative, and other explanations are possible.

Second, if the E7 residue served as a gate for ligand entry and exit, then the outward movement of the Gln-44 side chain would be expected to increase the rates of O_2 association and dissociation and decrease the fraction of geminate recombination by enhancing the rate of ligand escape. However, the Phe-55 and Trp-55 mutations cause the opposite effect, decreasing k'_{O2} and k_{O2} and increasing the fraction of internal rebinding. In addition, the outer Gln-44(E7) conformer does not create a significant opening to solvent, even though there is net movement away from the iron atom (Fig. 7). In WT sperm whale Mb, protonation of the imidazole side chain of His-64(E7) at low pH causes an upward and outward rotation into a truly open conformation, creating a direct channel from solvent to the iron atom (51). A similar opening is created by the Phe-46(CD4) to Val mutation in MbCO and deoxyMb (52), the binding of imidazole to metMb (53), and the binding of long chain isocyanides to deoxyMb (54–56). In contrast, access to the iron atom is still blocked in the outer Gln-44 conformer of Trp-55 CerHb (Fig. 7). In general, it is more difficult for the Gln-44 side chain to move out of the E7 channel because of the need for concerted rotations about C-α–C-β, C-β–C-γ, and C-γ–C-δ bonds and for disruption of two possible hydrogen bonding interactions for each of the N-ϵ and O-ϵ amide atoms. In contrast, the side chain of His-64 in Mb can rotate almost completely out of the E7 channel by changing only the torsion angle of the C-α–C-β bond (53), and the aromatic and secondary N atoms of the neutral imidazole side chain can only interact with one hydrogen bond donor and acceptor, respectively.

The third and fourth puzzles are that the O_2 affinities of WT CerHb and the position 55(E18) mutants are virtually identical (Table 2) and that stretching frequency of bound CO is unaffected by the Phe-55 and Trp-55 substitutions (Fig. 8 and below). These results suggest that the exact conformation of Gln-44(E7) has little effect on either the rate or equilibrium coefficients for ligand binding. The latter conclusion is partially

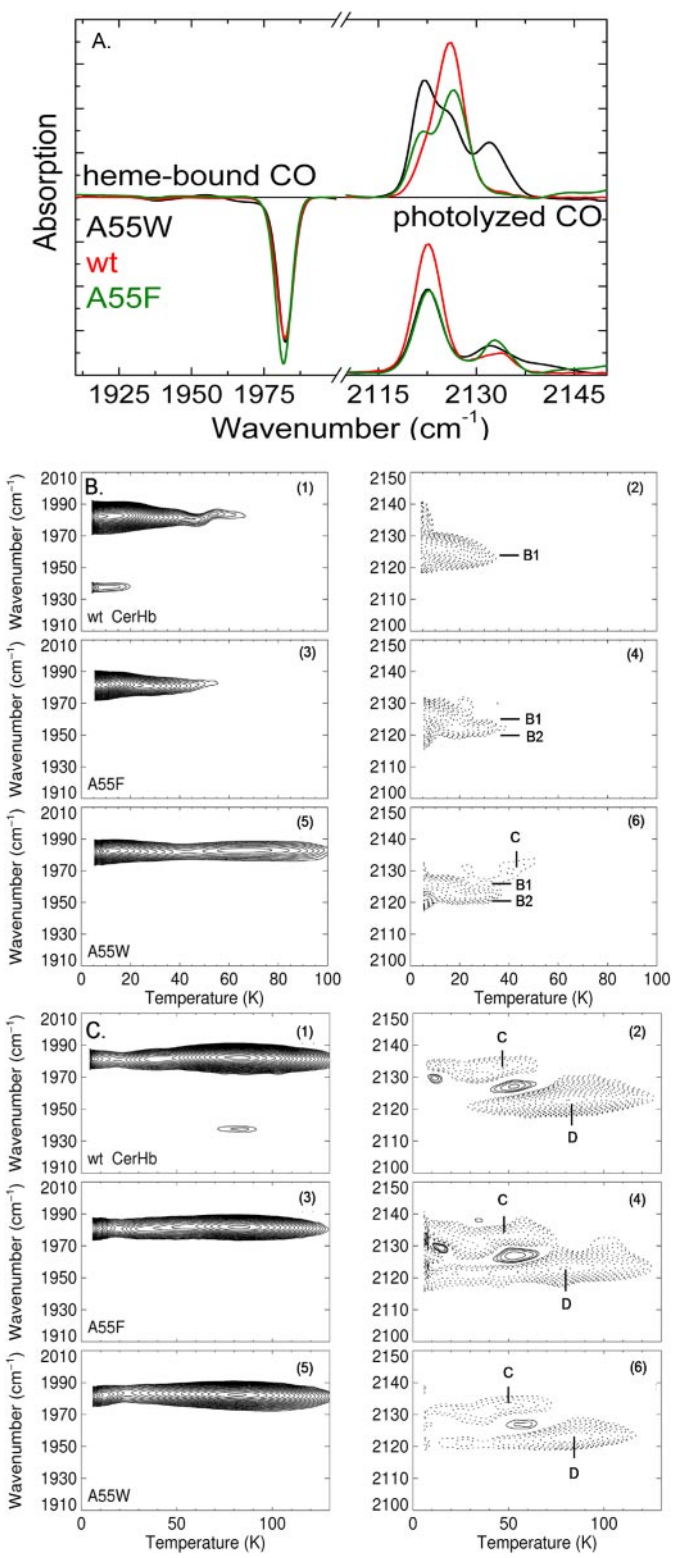

FIGURE 8. **FTIR photolysis difference spectra and TDS contour maps on Ala-55 mutants.** *A,* FTIR photolysis difference spectra of WT(Ala-55), Phe-55, and Trp-55 CerHbCO at 3 K. Absorption bands in the spectral region of heme-bound CO are plotted on the *left*, bands of photodissociated CO obtained after 1-s illumination at 3 K are plotted at *top right*, and those obtained after slow cooling from 160 to 3 K under continuous illumination are plotted at *lower right*. The heme-bound CO difference spectra for the slow cooling experiments are the same as those observed for 1-s illumination at 3 K. *B,* TDS contour maps calculated from measurements after 1 s illumination at 3 K. The *left* and *right columns* show the absorption changes in the bands of heme-bound and photolyzed CO, respectively, as a function of temperature. *Solid* and *dotted lines* indicate absorption increases and decreases, respectively. *C,* TDS contour maps calculated from data taken after slow cooling of the samples from 160 to 3 K under constant illumination. The states are labeled according to the scheme of Deng *et al.* (21); the proposed positions of states B and C are depicted in Fig. 9.

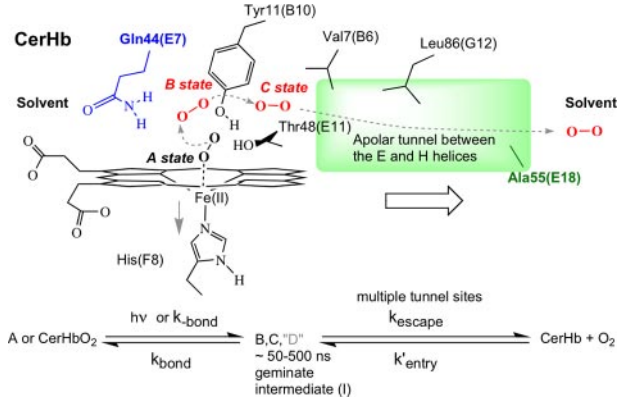

FIGURE 9. **Simple two-step mechanism for ligand binding to WT and Ala-55(E18) mutants of CerHb.** Deng *et al.* (21) have shown that there are at least three distinct transient docking sites for CO at 3–100 K and made tentative assignments to specific cavities within the protein. The B site is close to the iron atom in a cavity bounded by the porphyrin ring, Tyr-11 and Phe-10. The C site appears to be located further into the protein underneath Val-7. The D site (not shown) was suggested to be in the distal pocket close to Gln-44, Thr-48, and Tyr-11 and thought to be on a side path.

supported by the results for the position 44(E7) mutants in Table 1. The Ala-44, Val-44, and Leu-44 mutations have little effect on the ligand association rates and, unexpectedly, cause small to moderate decreases in the rate of O_2 dissociation. However, the Phe-44 and Trp-44 mutations cause marked decreases in k'_{O2} with little change in k_{O2}. The simplest interpretation of the latter result is that the large aromatic E7 side chains occupy the inner conformation and sterically hinder access to the iron atom and the bound ligand.

FTIR-TDS of Position 55 Mutants—We have shown previously that, when photodissociated at low temperatures, CO occupies several positions (denoted as B, C, and D) within the distal pocket of CerHb before migrating into the apolar channel (21). On the basis of the effects of distal pocket mutations, the B state was assigned to a position underneath Phe-10(B9) and Tyr-11(B10), directly above pyrrole C. The C state was identified as a position located further into the protein interior beneath Val-7(B6) and above the vinyl group of pyrrole B, just at the beginning of the apolar channel (21) (Fig. 9). The D state was tentatively assigned to a location within the distal pocket between Tyr-10(B10) and Gln-44(E7) and ≥5 Å above the heme plane.

At room temperature, photodissociated CO appears to equilibrate rapidly between those sites and the channel, and only a single, exponential geminate rebinding phase is observed on nanosecond time scales for the position 55 mutants and WT CerHb (Fig. 3). To examine the effects of blocking the channel entrance on ligand migration and rebinding from near the heme group in more detail, we measured low temperature FTIR photolysis difference spectra of WT, Phe-55, and Trp-55 CerHbCO (Fig. 8). These data serve to connect the initial dissociation events to the rates of ligand escape, entry, and bond formation measured at room temperature and to test more

directly whether or not the replacements of residue 55 have an effect on the reactivity of the heme iron atom and the innermost barrier to bond formation. Moreover, the low temperature FTIR data also allow assessing the functional consequences of the two conformers of Gln-44(E7) observed in the crystal structures of Phe-55 and Trp-55 CerHbO_2.

Two sets of similar experiments for WT, Phe-55, and Trp-55 CerHbCO are shown in Fig. 8. In the first protocol, the CerHbCO samples were cooled to 3 K in the dark and then illuminated for 1 s. Under these conditions, the photolyzed ligands are trapped mainly at the primary docking site B. In the second protocol, the CerHbCO samples were exposed to continuous laser illumination while being cooled slowly from 160 to 3 K. This protocol allows sampling of all internal transient ligand docking sites. In both types of experiments, absorbance difference spectra were calculated from transmission spectra measured before and after illumination (Fig. 8*A*). The negative features between 1900 and 2000 cm^{-1} represent the missing absorbance of the originally bound CO (A state bands), whereas the positive features between 2000 and 2150 cm^{-1} represent photodissociated CO trapped in different locations in or near the distal pocket.

As shown in Fig. 8*A*, the negative peaks representing bound CO occur at the same position, 1982 cm^{-1}, for WT CerHbCO and the two mutants. The presence of only a single CO stretching band for each sample reflects a structurally homogeneous binding site in the ligand-bound state. However, the photoproduct spectra at 3 K are different. A single B state band (B1) is observed for WT CerHbCO, suggesting that the dissociated ligand occupies a single site with a single orientation of the C-O molecule. Little or no conformational heterogeneity of the surrounding polar amino acids and the resultant electrostatic field at the CO ligand position is observed. In contrast, two peaks (B1 and B2) are observed for the photoproduct in Phe-55 CerHbCO, implying either two orientations, two distinct locations of the photolyzed CO, or two distinct conformations of the distal pocket amino acids. In the case of Trp-55 CerHbCO, three photoproduct bands (B1, B2, and C) are seen. Two are identical to the photoproduct states seen in WT (B1) and Phe-55 (B1 and B2) CerHbCO. The third, higher frequency band is associated with the secondary docking site C, which was observed previously for CerHb mutants in which Val-7(B6), Phe-10(B9), or Tyr-11(B10) were mutated to smaller amino acids (21) (Fig. 9). The appearance of this band in the Trp-55 mutant suggests that the large indole ring may cause minor perturbations along the E helix that reduce the volume of the distal pocket and site B. This reduction in volume might force the Gln-44 side chain outward and the dissociated ligand toward site C at the interior entrance to the apolar channel. However, this interpretation is speculative. After slow cooling from 160 to 3 K, all samples show still another photoproduct spectrum; the main band is associated with site D (Fig. 8*A*, *lower right*).

To examine thermally activated rebinding from the photoproduct states, the sample temperature was ramped upward at a rate of 5 mK/s, and an FTIR transmission spectrum was recorded every 1 K. Difference spectra were calculated for each successive temperature rise and then plotted as a function of both frequency and temperature as shown in Fig. 8*B*. The temperature at which the A state is regenerated (Fig. 8*B*, *left column, solid contour lines*) and the photoproduct states disappear (*right column, dashed contours*) provides a measure of the enthalpy barrier to return to the iron atom and bond formation. After a 1-s illumination (Fig. 8*B*), rebinding from both states B1 and B2 occurs at roughly the same low temperature, ~15–20 K, in WT CerHbCO and both position 55 mutants, indicating that these two bands are associated with ligands close to the iron atom. Thus, the Phe and Trp replacements have little effect on the inner barrier to CO rebinding from the B states. In the case of the Trp-55 mutant, the C state is partially populated, even after brief illumination at 3 K. As a result, a significant increase in the A state population occurs at ~65 K, reflecting rebinding from the C state.

TDS contour plots obtained after continuous illumination during cooling from 160 to 3 K are shown in Fig. 8*C*. In this case, most ligands are found trapped at sites C and D (21). Ligand rotation at site C occurs at the lowest temperatures, as seen from concomitant *solid* and *dotted contours* in Fig. 8*C*, *panels 2, 4,* and *6*. Ligand migration from site C to site D or rotation at site D occurs at roughly 40–50 K as observed by the disappearance of the band at ~2135 cm^{-1} and the positive contours at 2125 cm^{-1}. Rebinding from site C is maximal at 40 K under these conditions. The D state persists to higher temperatures; ligands in this side pathway rebind directly to the iron at ~80 K (21). The most striking observation is the similarity between the TDS patterns observed for WT CerHbCO and the Phe-55 and Trp-55 mutants, implying that the position 55(E18) mutations have little effect on the nature of the B, C, and D states and the enthalpy barriers between them. The small differences observed in Fig. 8, *B* and *C,* cannot account for the marked slowing of the overall rates of ligand binding and the increased fraction of geminate recombination observed on nanosecond time scales at room temperature as the size of the amino acid at position 55(E18) is increased (Fig. 3). Thus, the FTIR data strongly support our major conclusion that blocking the entrance to the apolar channel affects primarily the rates of ligand entry into and exit from the protein.

DISCUSSION

The E7 Gate Versus the Apolar Channel—The effects of mutagenesis of Gln-44(E7) in CerHb are complex and markedly different from those observed for the same set of replacements at the E7 position in sperm whale Mb (Table 1 and Fig. 2). Replacement of Gln-44 with smaller apolar amino acids results in small decreases in both the association and dissociation rates for O_2 binding to CerHb. In contrast, when His-64(E7) is replaced with Ala, Val, or Leu in sperm whale Mb, 10–1000-fold increases in k'_{O2} and k_{O2} are observed. These results argue against an E7 gate pathway for ligand movement into CerHb. The His-44 and Phe-44 CerHb mutants and one of the conformers of the Trp-44 mutant do show significant decreases in k'_{O2}, which could be interpreted as due to blockage of the E7 gate. However, the dissociation rate coefficients for the Phe-44 mutant and that for one of the Trp-44 conformers are large and equal to k_{O2} for WT CerHbO_2.

Thus, the results for mutagenesis of Gln-44(E7) are equivocal with respect to defining the pathway for ligand movement into CerHb. Rather than blocking entry and exit, the decreases in k'_{O2} caused by the His-44, Phe-44, and Trp-44 mutations are more easily interpreted as due to direct hindrance of bond formation with the iron atom by the large aromatic side chains. This idea is supported by the 10-fold decreases in the bimolecular rates for CO binding caused by the Q44H, Q44F, and Q44W mutations (k'_{CO} values in Table 1). The limiting step for CO binding to most heme proteins is the rate of internal bond formation, which is at least 10 to 1000-fold smaller than the rates of internal bond formation for O_2 and NO, respectively (48). Thus, the large ~10-fold decreases in k'_{CO} observed for the His-44, Phe-44, and Trp-44 mutants are consistent with sterically hindered access to the iron atom. This interpretation is further supported by the small fractions of geminate recombination observed for WT CerHbCO and all the position 44(E7) mutants shown in Fig. 3*A*. If the large aromatic side chains were blocking escape, the fraction of internal rebinding should increase as the size of the amino acid at the E7 position increases. However, the Phe-44 and His-44 mutants show the least amount of geminate CO recombination; the Leu-44 and Val-44 mutants show the greatest amount; and none of the mutants are significantly different from WT CerHbCO (Fig. 3*A*).

In contrast to the E7 replacements, the Ala-55(E18) mutations show a pattern of kinetic effects remarkably consistent with this position being at the entrance to ligand movement into CerHb. Both the association and dissociation rate coefficients for O_2 binding decrease uniformly with increasing side chain size, and there is little change in overall ligand affinity (Table 2 and Fig. 4). As shown in Fig. 3, *B* and *A,* and Table 2, the fraction of geminate recombination increases with increasing size of the amino acid at position 55, whereas the rate of geminate recombination decreases. These results demonstrate qualitatively that the increase in internal recombination is because of a decrease in the rate of ligand escape as would be expected if the exit to solvent were blocked by the larger amino acids at the E18 position.

Simple Mechanism for Ligand Binding to CerHb—The two-step mechanism shown in Fig. 9 was adopted to determine more quantitatively the effects of the 55 mutations on the rates of ligand entry and exit. Following a strategy that was developed earlier to examine secondary ligand docking sites in Mb variants (12, 57), Deng *et al.* (21) have shown that multiple transient docking sites also exist in the distal pocket of CerHb and are separated by relatively small enthalpy barriers against ligand migration. These discrete photoproduct intermediates are easily visualized in FTIR-TDS experiments at cryogenic temperatures (3–160 K); the locations of these states shown in Fig. 9 were assigned by the effects of mutagenesis on the transitions between them (21). However, at room temperature, simple exponential geminate rebinding is observed, suggesting that only a single intermediate needs to be considered on time scales of 10–2000 ns.

At ambient temperatures, both geminate and overall ligand binding to CerHb can be analyzed in terms of three reactions as follows: 1) photolysis to the intermediate state, where the ligand is located in transient equilibrium between the C, B, and channel positions; 2) rebinding to the iron atom from this intermediate state at a rate equal to k_{bond}; and 3) escape from the intermediate state out through the channel past the Ala-55(E18) position at a rate equal to k_{escape}. The fraction and rate of geminate rebinding, F_{gem} and k_{gem}, are given by Equation 3,

$$F_{gem} = \frac{k_{bond}}{k_{bond} + k_{escape}},\ k_{gem} = k_{bond} + k_{escape} \qquad \text{(Eq. 3)}$$

$$k_{bond} = k_{gem}F_{gem},\ k_{escape} = k_{gem}(1 - F_{gem})$$

The fractions and rates of internal recombination are obtained by fitting the observed geminate time courses to a single exponential expression, where the first-order rate is k_{gem}, and the normalized amplitude for rebinding and the offset are equal to F_{gem} and $1 - F_{gem}$, respectively (48). These parameters can then be used to compute k_{bond} and k_{escape} as shown in Equation 3. An expression for the overall bimolecular rate coefficient for ligand binding, k'_X, where X is the ligand (O_2, CO, NO, etc.), can be obtained by assuming a steady-state approximation ($d\langle I\rangle/dt = 0$) for the intermediate on μs and ms time scales. Under these conditions, k'_X is given by Equation 4,

$$k'_x = k'_{entry}\frac{k_{bond}}{k_{bond} + k_{escape}} = k'_{entry}F_{gem} \qquad \text{(Eq. 4)}$$

$$k'_{entry} = \frac{k'_x}{F_{gem}}$$

Equations 3 and 4 and the measured kinetic parameters for O_2 and CO binding in Table 2 were used to compute estimates of k'_{entry}, k_{escape}, and k_{bond} for ligand binding to WT CerHb and the four position 55 mutants. The results are shown in Table 3. These parameters provide a self-consistent interpretation of both O_2 and CO binding. The estimated value of k_{bond} for O_2 rebinding is, as expected, roughly 10 times greater than that for CO, ~50 μs^{-1} *versus* ~4 μs^{-1}. Both values of k_{bond} are independent of changes at the position 55(E18), demonstrating that the amino acid at this remote location does not influence the reaction at the iron atom. In contrast, the values of k'_{entry} and k_{escape} are roughly independent of the ligand, but both rates decrease over 10-fold as the size of the position 55 amino acid is increased (Table 3). The correspondence of the absolute values of k'_{entry} and k_{escape} calculated using the O_2 and CO data is remarkably good, considering that it is difficult to determine the exact values of k_{gem} and F_{gem} for O_2. For this ligand, significant geminate rebinding is occurring during the laser excitation pulse, and the fitted rate is approaching the decay rate of the pulse light intensity.

Bimolecular rates of NO binding were measured to verify the computed values of k'_{entry}. NO is expected to show F_{gem} values $\geq$0.95, and we verified that CerHbNO has an extremely small quantum yield for complete photodissociation to the solvent (data not shown). Thus k'_{NO} should be approximately equal to k'_{entry}. As shown in Table 3 and the Fig. 5, *inset*, there is a strong linear correlation between k'_{NO} and k'_{entry}. However, the calculated values of k'_{entry} appear to be ~2-fold greater than k'_{NO} for WT and Val-55 CerHb. The cause of this discrepancy is

probably the oversimplification inherent in the two-step model. For WT and Val-55 CerHb, the extent of geminate recombination is small and the rate is large and difficult to define. In addition, there are probably multiple steps that cannot be easily visualized using a 9-ns excitation pulse. In these proteins, the internal channel is open to solvent, and, as a result, the photodissociated ligands are not easily trapped in an intermediate state. More complex expressions define the overall rate coefficient when contributions from the rates of interconversion of the B and C states are incorporated into the steady-state expression for k'_{entry}. Evidence for these inner ligand transitions is seen in the kinetic data for mutations in the B and C sites (data not shown), complicating our larger mapping study of the entire pathway. However, regardless of the exact interpretation, there is a very good correspondence between k'_{NO} and the calculated values of k'_{entry} for the larger 55 mutants (Table 3), which supports our view that ligands enter CerHb primarily through the apolar channel.

Perhaps the strongest argument in favor of the mechanism in Fig. 9 for interpreting the effects of the position 55 mutants is the independence of the estimated equilibrium constant, K_{entry}, for noncovalent capture of ligands in the intermediate state (*i.e.* in the channel and the space associated with state B and C). The average computed value is $\sim 9.1 \pm 2.0\ M^{-1}$ for WT and the four 55 mutant CerHbs and does not vary with either ligand or the size of the residue at the entrance to the apolar channel (Table 3). The lack of dependence on the amino acid at position 55(E18) fits with the structures of WT, Phe-55, and Trp-55, all of which show equivalent channel volumes of ~ 56 Å^3. The value of K_{entry} for ligand capture in WT sperm whale Mb is $\sim 5.5 \pm 1.8\ M^{-1}$, implying that the apolar channel in CerHb provides almost twice the volume for noncovalent ligand binding than the distal pocket and xenon cavities in mammalian Mb (3). However, in WT sperm whale Mb, a water molecule is present in the distal pocket reducing the effective volume for noncovalent capture. When this water is removed by replacing His-64(E7) with Leu, the value of K_{entry} for sperm whale Mb increases to $\sim 10\ M^{-1}$, and similar values were estimated for Val-64 and Phe-64 Mb (3). Thus, when the water is removed, the functional capture volume in Mb, as measured by the equilibrium constant for noncovalent ligand binding, is similar to that in the CerHb channel.

The Apolar Channel Is the Route of Entry—Taken together the kinetic and structural data for the position 55(E18) mutants demonstrate unambiguously that the major pathway for ligand entry and exit in CerHb is the apolar channel between the E and H helices, which is shown in Figs. 1, 6, and 9. Increasing the size of the amino acid at this position increases the free energy barrier to ligand movement from the solvent interface into the apolar channel. Changing the size of the barrier only affects the rates of entry and exit and not the rate of iron-ligand bond formation, the equilibrium constant for noncovalent ligand capture, and the overall affinity of CerHb for ligands. The lack of further decreases in either k'_{entry} or k_{escape} as the size of residue 55 is increased from Leu to Phe to Trp suggests that the small, limiting values of these parameters, $\sim 50\ \mu M^{-1}\ s^{-1}$ and $\sim 6\ \mu s^{-1}$, respectively (Table 3), may represent the rates of ligand movement through the E7 gate. The rates for the Trp-55 and Phe-55 mutants are remarkably similar to the values estimated for entry into and exit from WT sperm whale Mb which clearly uses the E7 channel ($k'_{entry} \approx 34 \pm 7\ \mu M^{-1}\ s^{-1}$ and $6.3 \pm 1\ \mu s^{-1}$ (3)). However, our current sets of single mutants and FTIR data cannot define the location of alternative pathways.

Physiology and Evolution—CerHb is part of a group of invertebrate and microbial globins, which have ligand-binding sites containing a Tyr(B10) and Gln(E7) motif (58). Domain 1 of *Ascaris suum* hemoglobin is a representative of the invertebrate Tyr(B10)/Gln(E7) proteins, which normally have ultra-high affinities for O_2 ($P_{50} \approx 0.003$ to $0.1\ \mu M$) due both to favorable proximal geometry and strong hydrogen bonds between the Tyr(B10) and Gln(E7) side chains and the bound O_2 (31, 59–61). However, CerHb is a neuronal globin that has an oxygen storage function (30, 62). It takes up and stores O_2 when the worm is in seawater and then releases it to nerve tissue when the organism burrows into mud flats and becomes anoxic (30). Thus, CerHb evolved under strong selective pressure to have a Mb-like O_2 affinity, with a $P_{50} \approx 1\ \mu M$, and large rates of O_2 uptake and release. We showed previously that the moderate O_2 affinity is because of the presence of Thr-48 at the E11 position, which is an apolar amino acid in most other animal globins (32). The need for rapid rates of O_2 exchange during transient periods of hypoxia appears to have led to the loss of the A helix and concomitant creation of a large apolar channel between the E and H helices coupled with the loss of the A helix. This channel allows dramatically high rates of O_2 binding to and release from CerHb compared with other proteins containing the Tyr(B10)/Gln(E7) motif. For example, Tyr-29(B10)/Gln-64(E7) Mb has an O_2 affinity ($K_{O2} \approx 1.9\ \mu M^{-1}$) similar to CerHb but shows rate coefficients that are 100-fold smaller, k'_{O2} and $k_{O2} = 2.8\ \mu M^{-1}\ s^{-1}$ and $1.6\ s^{-1}$, respectively, and *A. suum* Hb shows even smaller rate coefficients for O_2 binding (31). Thus, CerHb provides a clear example of convergent evolution to obtain an Mb-like function using electrostatic destabilization of bound O_2 to decrease O_2 affinity (32) and loss of the A helix to create a new, more efficient pathway for ultra fast ligand entry and exit.

REFERENCES

1. Kendrew, J. C. (1963) *Science* **139,** 1259–1266
2. Perutz, M. F., Bolton, W., Diamond, R., Muirhead, H., and Watson, H. C. (1964) *Nature* **203,** 687–690
3. Scott, E. E., Gibson, Q. H., and Olson, J. S. (2001) *J. Biol. Chem.* **276,** 5177–5188
4. Srajer, V., Ren, Z., Teng, T. Y., Schmidt, M., Ursby, T., Bourgeois, D., Pradervand, C., Schildkamp, W., Wulff, M., and Moffat, K. (2001) *Biochemistry* **40,** 13802–13815
5. Schotte, F., Soman, J., Olson, J. S., Wulff, M., and Anfinrud, P. A. (2004) *J. Struct. Biol.* **147,** 235–246
6. Schmidt, M., Nienhaus, K., Pahl, R., Krasselt, A., Anderson, S., Parak, F., Nienhaus, G. U., and Srajer, V. (2005) *Proc. Natl. Acad. Sci. U. S. A.* **102,** 11704–11709
7. Bourgeois, D., Vallone, B., Arcovito, A., Sciara, G., Schotte, F., Anfinrud, P. A., and Brunori, M. (2006) *Proc. Natl. Acad. Sci. U. S. A.* **103,** 4924–4929
8. Aranda, R. T., Levin, E. J., Schotte, F., Anfinrud, P. A., and Phillips, G. N., Jr. (2006) *Acta Crystallogr. Sect. D Biol. Crystallogr.* **62,** 776–783
9. Olson, J. S., Soman, J., and Phillips, G. N., Jr. (2007) *IUBMB Life* **59,** 552–562
10. Olson, J. S., and Ghosh, A. (2008) in *The Smallest Biomolecules: Perspectives on Heme-Diatomic Interactions* (Ghosh, A., ed) pp. 3–17, Elsevier

Science Ltd., London
11. Huang, X., and Boxer, S. G. (1994) *Nat. Struct. Biol.* **1,** 226–229
12. Nienhaus, K., Deng, P., Kriegl, J. M., and Nienhaus, G. U. (2003) *Biochemistry* **42,** 9633–9646
13. Frauenfelder, H., McMahon, B. H., Austin, R. H., Chu, K., and Groves, J. T. (2001) *Proc. Natl. Acad. Sci. U. S. A.* **98,** 2370–2374
14. Nienhaus, K., Olson, J. S., Franzen, S., and Nienhaus, G. U. (2005) *J. Am. Chem. Soc.* **127,** 40–41
15. Nienhaus, K., Ostermann, A., Nienhaus, G. U., Parak, F. G., and Schmidt, M. (2005) *Biochemistry* **44,** 5095–5105
16. Lim, M., and Anfinrud, P. A. (2005) *Methods Mol. Biol.* **305,** 243–260
17. Cao, W., Ye, X., Georgiev, G. Y., Berezhna, S., Sjodin, T., Demidov, A. A., Wang, W., Sage, J. T., and Champion, P. M. (2004) *Biochemistry* **43,** 7017–7027
18. Vos, M. H. (2008) *Biochim. Biophys. Acta* **1777,** 15–31
19. Wittenberg, J. B., Bolognesi, M., Wittenberg, B. A., and Guertin, M. (2002) *J. Biol. Chem.* **277,** 871–874
20. Milani, M., Pesce, A., Ouellet, Y., Ascenzi, P., Guertin, M., and Bolognesi, M. (2001) *EMBO J.* **20,** 3902–3909
21. Deng, P., Nienhaus, K., Palladino, P., Olson, J. S., Blouin, G., Moens, L., Dewilde, S., Geuens, E., and Nienhaus, G. U. (2007) *Gene* (*Amst.*) **398,** 208–223
22. Bidon-Chanal, A., Marti, M. A., Crespo, A., Milani, M., Orozco, M., Bolognesi, M., Luque, F. J., and Estrin, D. A. (2006) *Proteins* **64,** 457–464
23. Pesce, A., Couture, M., Dewilde, S., Guertin, M., Yamauchi, K., Ascenzi, P., Moens, L., and Bolognesi, M. (2000) *EMBO J.* **19,** 2424–2434
24. Milani, M., Pesce, A., Nardini, M., Ouellet, H., Ouellet, Y., Dewilde, S., Bocedi, A., Ascenzi, P., Guertin, M., Moens, L., Friedman, J. M., Wittenberg, J. B., and Bolognesi, M. (2005) *J. Inorg. Biochem.* **99,** 97–109
25. Milani, M., Pesce, A., Ouellet, H., Guertin, M., and Bolognesi, M. (2003) *IUBMB Life* **55,** 623–627
26. Crespo, A., Marti, M. A., Kalko, S. G., Morreale, A., Orozco, M., Gelpi, J. L., Luque, F. J., and Estrin, D. A. (2005) *J. Am. Chem. Soc.* **127,** 4433–4444
27. Bidon-Chanal, A., Marti, M. A., Estrin, D. A., and Luque, F. J. (2007) *J. Am. Chem. Soc.* **129,** 6782–6788
28. Pesce, A., Nardini, M., Dewilde, S., Ascenzi, P., Riggs, A. F., Yamauchi, K., Geuens, E., Moens, L., and Bolognesi, M. (2001) *Acta Crystallogr. Sect. D Biol. Crystallogr.* **57,** 1897–1899
29. Pesce, A., Nardini, M., Dewilde, S., Geuens, E., Yamauchi, K., Ascenzi, P., Riggs, A. F., Moens, L., and Bolognesi, M. (2002) *Structure* (*Lond.*) **10,** 725–735
30. Vandergon, T. L., Riggs, C. K., Gorr, T. A., Colacino, J. M., and Riggs, A. F. (1998) *J. Biol. Chem.* **273,** 16998–17011
31. Draghi, F., Miele, A. E., Travaglini-Allocatelli, C., Vallone, B., Brunori, M., Gibson, Q. H., and Olson, J. S. (2002) *J. Biol. Chem.* **277,** 7509–7519
32. Pesce, A., Nardini, M., Ascenzi, P., Geuens, E., Dewilde, S., Moens, L., Bolognesi, M., Riggs, A. F., Hale, A., Deng, P., Nienhaus, G. U., Olson, J. S., and Nienhaus, K. (2004) *J. Biol. Chem.* **279,** 33662–33672
33. Rohlfs, R. J., Mathews, A. J., Carver, T. E., Olson, J. S., Springer, B. A., Egeberg, K. D., and Sligar, S. G. (1990) *J. Biol. Chem.* **265,** 3168–3176
34. Olson, J. S., Foley, E. W., Maillett, D. H., and Paster, E. V. (2003) *Methods Mol. Med.* **82,** 65–91
35. Schweers, R. L. (2003) Electrostatic regulation of oxygen and carbon monoxide binding in the alpha and beta subunits of recombinant human hemoglobin. Ph.D. thesis, Rice University, Houston
36. Olson, J. S. (1981) *Methods Enzymol.* **76,** 631–651
37. Berendzen, J., and Braunstein, D. (1990) *Proc. Natl. Acad. Sci. U. S. A.* **87,** 1–5
38. Mourant, J. R., Braunstein, D. P., Chu, K., Frauenfelder, H., Nienhaus, G. U., Ormos, P., and Young, R. D. (1993) *Biophys. J.* **65,** 1496–1507
39. Nienhaus, K., and Nienhaus, G. U. (2008) *Methods Enzymol.* **437,** 347–378
40. Leslie, A. G. M. (2003) MOSFLM User Guide Mosflm Version 6.2.3, MRC Laboratory of Molecular Biology, Cambridge, UK
41. Evans, P. R. (2004) *Proceedings of the CCP4 Study Weekend, on Data Collection and Processing,* pp. 114–122, CLRC Daresbury Laboratory, Warrington, UK
42. Vagin, A., and Teplyakov, A. (1997) *J. Appl. Crystallogr.* **30,** 1022–1025
43. Potterton, L., McNicholas, S., Krissinel, E., Gruber, J., Cowtan, K., Emsley, P., Murshudov, G. N., Cohen, S., Perrakis, A., and Noble, M. (2004) *Acta Crystallogr. Sect. D Biol. Crystallogr.* **60,** 2288–2294
44. Collaborative, Computational Project Number 4 (1994) *Acta Crystallogr. Sect. D Biol. Crystallogr.* **50,** 760–763
45. Murshudov, G. N., Vagin, A. A., and Dodson, E. J. (1997) *Acta Crystallogr. Sect. D Biol. Crystallogr.* **53,** 240–255
46. Emsley, P., and Cowtan, K. (2004) *Acta Crystallogr. Sect. D Biol. Crystallogr.* **60,** 2126–2132
47. Berman, H. M., Westbrook, J., Feng, Z., Gilliland, G., Bhat, T. N., Weissig, H., Shindyalov, I. N., and Bourne, P. E. (2000) *Nucleic Acids Res.* **28,** 235–242
48. Olson, J. S., and Phillips, G. N., Jr. (1996) *J. Biol. Chem.* **271,** 17593–17596
49. Carver, T. E., Rohlfs, R. J., Olson, J. S., Gibson, Q. H., Blackmore, R. S., Springer, B. A., and Sligar, S. G. (1990) *J. Biol. Chem.* **265,** 20007–20020
50. Laskowski, R. A. (1995) *J. Mol. Graphics* **13,** 323–330
51. Yang, F., and Phillips, G. N., Jr. (1996) *J. Mol. Biol.* **256,** 762–774
52. Lai, H. H., Li, T., Lyons, D. S., Phillips, G. N., Jr., Olson, J. S., and Gibson, Q. H. (1995) *Proteins* **22,** 322–339
53. Bolognesi, M., Cannillo, E., Ascenzi, P., Giacometti, G. M., Merli, A., and Brunori, M. (1982) *J. Mol. Biol.* **158,** 305–315
54. Johnson, K. A., Olson, J. S., and Phillips, G. N., Jr. (1989) *J. Mol. Biol.* **207,** 459–463
55. Johnson, K. A. (1993) High-resolution X-ray structures of myoglobin- and hemoglobin-alkyl isocyanide complexes. Ph.D. thesis, Rice University, Houston
56. Smith, R. D. (1999) Correlations between bound n-alkylisocyanide orientations and pathways for ligand binding in recombinant myoglobins. Ph.D. thesis, Rice University, Houston
57. Nienhaus, K., Deng, P., Olson, J. S., Warren, J. J., and Nienhaus, G. U. (2003) *J. Biol. Chem.* **278,** 42532–42544
58. Weber, R. E., and Vinogradov, S. N. (2001) *Physiol. Rev.* **81,** 569–628
59. Gibson, Q. H., Regan, R., Olson, J. S., Carver, T. E., Dixon, B., Pohajdak, B., Sharma, P. K., and Vinogradov, S. N. (1993) *J. Biol. Chem.* **268,** 16993–16998
60. Goldberg, D. E. (1999) *Chem. Rev.* **99,** 3371–3378
61. Huang, S., Huang, J., Kloek, A. P., Goldberg, D. E., and Friedman, J. M. (1996) *J. Biol. Chem.* **271,** 958–962
62. Geuens, E., Dewilde, S., Hoogewijs, D., Pesce, A., Nienhaus, K., Nienhaus, G. U., Olson, J., Vanfleteren, J., Bolognesi, M., and Moens, L. (2004) *IUBMB Life* **56,** 653–656
63. Laskowski, R. A., and MacArthur, M. W. (1993) *J. Appl. Crystallogr.* **26,** 283–291

The Apolar Channel in *Cerebratulus lacteus* Hemoglobin Is the Route for O_2 Entry and Exit

Mallory D. Salter, Karin Nienhaus, G. Ulrich Nienhaus, Sylvia Dewilde, Luc Moens, Alessandra Pesce, Marco Nardini, Martino Bolognesi and John S. Olson

J. Biol. Chem. 2008, 283:35689-35702.
doi: 10.1074/jbc.M805727200 originally published online October 7, 2008
